Journal of *Marine Science and Engineering*

MDPI

Article

Six-DOF CFD Simulations of Underwater Vehicle Operating Underwater Turning Maneuvers

Kunyu Han [1,2], Xide Cheng [1,2,*], Zuyuan Liu [1,2,*], Chenran Huang [3], Haichao Chang [1,2], Jianxi Yao [1,2] and Kangli Tan [3]

[1] Key Laboratory of High Performance Ship Technology, Wuhan University of Technology, Ministry of Education, Wuhan 430063, China; kyhan@whut.edu.cn (K.H.); changhaichao@whut.edu.cn (H.C.); yao@whut.edu.cn (J.Y.)
[2] School of Naval Architecture, Ocean and Energy Power Engineering Wuhan University of Technology, Wuhan 430063, China
[3] China Ship Development and Design Center, Wuhan 430064, China; hubcp520@163.com (C.H.); tankangli7012020@126.com (K.T.)
* Correspondence: xdcheng@whut.edu.cn (X.C.); wtulzy@whut.edu.cn (Z.L.)

Abstract: Maneuverability, which is closely related to operational performance and safety, is one of the important hydrodynamic properties of an underwater vehicle (UV), and its accurate prediction is essential for preliminary design. The purpose of this study is to analyze the turning ability of a UV while rising or submerging; the computational fluid dynamics (CFD) method was used to numerically predict the six-DOF self-propelled maneuvers of submarine model BB2, including steady turning maneuvers and space spiral maneuvers. In this study, the overset mesh method was used to deal with multi-body motion, the body force method was used to describe the thrust distribution of the propeller at the model scale, and the numerical prediction also included the dynamic deflection of the control planes, where the command was issued by the autopilot. Then, this study used the published model test results of the tank to verify the effectiveness of the CFD prediction of steady turning maneuvers, and the prediction of space spiral maneuvers was carried out on this basis. The numerical results show that the turning motion has a great influence on the depth and pitch attitude of the submarine, and a "stern heavier" phenomenon occurs to a submarine after steering. The underwater turning of a submarine can not only reduce the speed to brake but also limit the dangerous depth. The conclusion is of certain reference significance for submarine emergency maneuvers.

Keywords: 6-DOF; CFD; self-propelled; steady turning maneuver; space spiral maneuver; autopilot

Citation: Han, K.; Cheng, X.; Liu, Z.; Huang, C.; Chang, H.; Yao, J.; Tan, K. Six-DOF CFD Simulations of Underwater Vehicle Operating Underwater Turning Maneuvers. *J. Mar. Sci. Eng.* **2021**, *9*, 1451. https://doi.org/10.3390/jmse9121451

Academic Editor: Alessandro Ridolfi

Received: 25 November 2021
Accepted: 15 December 2021
Published: 18 December 2021

1. Introduction

Maneuverability, an important hydrodynamic property of underwater vehicles (UVs), is closely related to the safety and combat capability of UV functions. Conventionally, a UV usually adjusts the control unit by transmitting signals from the control system and changes or maintains the established course according to the requirements of the mission. The signals transmitted to different control units are affected by the maneuverability of UVs. Therefore, the accurate estimation of the maneuver performance of the UV plays a crucial role in the design of the control system and the ability of the UV to achieve the desired trajectory during the tasks. Maneuverability can be studied by means of a numerical technique and test procedures or a combination of the two. The former includes the method based on the hydrodynamic coefficients and self-propulsion model test prediction. The hydrodynamic coefficients are brought into the motion equations to simulate the maneuvers of UVs (Gertler and Hagen [1], 1967; Feldman [2], 1979). It has been widely used as it quickly predicts the ability of the setting coefficients and simulation time in maneuver predictions; however, the coupling effects of various factors in maneuvers are ignored due to several simplifications (Huang [3], 2018). More importantly, the prediction

was limited due to the fact this method cannot capture the changes of flow and vorticity in the maneuvers (Bettle [4], 2013); therefore, it can only be used as a tool and method to predict the maneuvering trajectory and attitude of the UV in early research. Hence, this study proposes a numerical prediction method based on a self-propulsion model that involves a body force propeller and the response of an autopilot controller to improve the accuracy of the simulations.

The UV model test was used to verify the simulation prediction results based on coefficients (Itard [5], Issac et al. [6], Jun et al. [7], Toxopeus et al. [8], Quick and Woodyatt [9]); however, this test method generally has limitations due to its cost and the need for specialized equipment and facilities. With the improvement of computational fluid dynamics (CFD) and high-performance computing (HPC) capabilities, CFD numerical simulation based on self-propulsion model tests provides a new direction for maneuverability prediction and research and is well suited as a complement to experimental studies, although validation may require experimental results.

Chase [10] designed a one-DOF (degree of freedom) self-propelled CFD simulation for a full appendage general submarine SUBOFF equipped with a fixed control plane and rotating propeller (Groves [11]). The CFD results are compared with the self-propelled model tank test results to verify that the propulsion performance of the two methods is in good agreement at the speed of 1.75 m/s (thrust coefficient K_T, torque coefficient K_Q, propeller efficiency η). However, since the model test and numerical simulation of the propeller require significant computational costs, the study was limited to calculating the trajectory velocity and acceleration of the UV at one-DOF only. Meanwhile, Chase suggested that the real propeller model in the numerical simulation of the steering motion could be replaced with a body force propeller model to greatly reduce the computational time and cost. Chase [12] carried out a three-DOF zig-zag maneuver simulation of SUBOFF in the horizontal plane. As there were no test results of free-sailing self-propulsion, he adopted two methods (direct simulation of the propeller and body force to replace the propeller) to compare the accuracy. The results show that the body force method can replace the propeller effect well. At the same time, the research pointed out that the potential of this method and it can be adapted to simulate a rising maneuver.

In an earlier study, the UV maneuver simulations mainly aimed at simple planar motions that were three-DOF motions (Broglia et al. [13]; Dubbioso et al. [14]; Feng et al. [15]; Yasemin et al. [16]). With the enhancement of computing performance and the development of dynamic grid and other technologies, the simulation of UV maneuvers took the ship, propeller and controlling planes into consideration at the same time. Meanwhile, more attention was paid to the attitude of a UV during navigation. The full six degrees of the self-propelled maneuvering motion appendage control algorithm and extensible performance are the basis of the implementation of free navigation maneuvering simulation.

Carrica [17] carried out a series of six-DOF numerical simulations of the general submarine model Joubert BB2 (designed by MARIN) based on self-propulsion and self-sailing tests, including self-propulsion near the surface and at depth, turning circles, vertical and horizontal zigzag maneuvers at depth, and rise to the surface maneuvers with stops by crash-back. The calculation was modeled after the principle of the autopilot in the test model. In all conditions, the autopilot controlled the propeller and control plane and used the vertical command to control pitch and depth and the horizontal command to control the yaw and sway of BB2. The results show that the CFD method can predict the self-propulsion maneuver distinctions well within 5%, and the motion and speed can be predicted under free-sailing conditions well. The study also pointed out that the attitude of the submarine controlled by autopilot is the most difficult part to predict, and the command correlation of the controller in the test is difficult to replicate completely.

Kim [18] explored the ability of the CFD method to predict the six-DOF free-sailing maneuver of a fully appendaged UV based on the commercial software STAR-CCM+ according to research by Bettle [4] and Coe [19]. The study adopted movable control planes and a body force propeller represented by an actuator disk incorporating predetermined

propulsion properties. The aft control planes were X-shaped and consisted of four independent planes; the horizontal and vertical motion of the UV was controlled by autopilot using a proportional-differential (PD) controller that has proportional and differential coupling control parameters. The validation of the experimental data provided by Overpelt [20] established the credibility of the CFD free-running simulation results.

A CFD study of a UV is surely more complicated and difficult compared with surface ships due to the increase in the vertical degrees of freedom (pitch and heave). Since vertical control is related to the safe navigation of a UV, its prediction should be important as well. Zhou [21] simulated a submarine's rising maneuvers in still water and waves and analyzed the feasibility and potential of a submarine's emergency buoyancy maneuverability in a harsh environment through direct numerical simulation. Wu [22] used the multi-block hybrid grid and removable region method to simulate a UV-forced self-propelled diving maneuver, summarized and analyzed the maneuverability of a UV diving motion qualitatively. Carrica [23] used dynamic grid technology to numerically predict a submarine's vertical zigzag maneuverability and verified the feasibility of the CFD calculation with experimental results.

This study aimed to comprehensively analyze the turning ability as well as the rising and submergence abilities in the vertical direction. First, the 6-DOF self-propelled turning maneuver of a general submarine is simulated, the movable control planes and a body force propeller for free-sailing are adopted, and the deflections of the control planes are determined, by autopilot, that the settings are based on the test; the results showed that the 6-DOF CFD maneuvering simulation method can predict a vehicle's speed and maneuvering characteristics well. Then, this study presents the maneuvering performance of the submarine under spiral rising and submergence conditions, and the space turning performance of the submarine is verified as well. The operational performance and safe navigation performance of the submarine are discussed based on the trajectory and attitude of the submarine under two operating conditions.

2. Materials and Methods

2.1. Model and Coordinate

The target underwater vehicle in the present study is the generic submarine Joubert BB2, which is introduced as an international benchmark for submarines. This submarine is in the modern generic SSK-class; it was designed by Professor Joubert [24,25] from DSTO in Australia, and MARIN modified the original geometry later; the geometry is available from MARIN in several solid body formats, as shown by Watt [26]. The full-scale length is 70.2 m, and the appendages include a sail, x-configuration stern control planes and a casing on top. The model scale BB2 geometry with a scale factor (λ) of 18.348 was utilized in the study according to Froude scaling laws, as the model is 3.826 m long. There is a six-bladed stock propeller (MARIN 7371R) attached for propulsion. Table 1 shows the main parameters of the BB2 model, and the entire model (including all appendages) is reported in Figure 1.

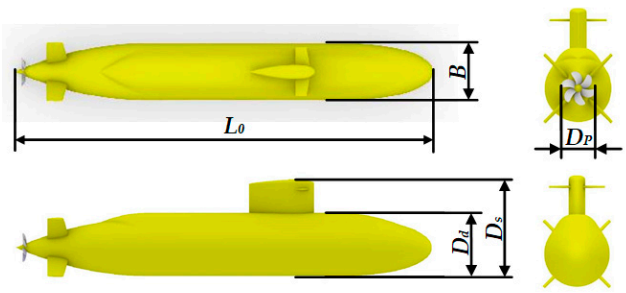

Figure 1. BB2 geometry (hull, propeller, rudder).

Table 1. Main parameters of BB2 (model scale 1:18.348). Mass properties of the scaled BB2 submarine by a factor of 18.348; the longitudinal and vertical CG was measured from the front nose tip and the keel, and the moments of inertia (i.e., r_x, r_y and r_z) are about the CG.

Model Parameters	Symbol	Scale (Full)	Scale (Model)
Length	$L_0(m)$	70.2	3.8260
Beam	$B(m)$	9.6	0.5232
Draft to Deck	$D_d(m)$	10.6	0.5777
Draft to Sail Top	$D_s(m)$	16.2	0.8829
Propeller Diameter	$D_p(m)$	5	0.273
Displacement	$\Delta(tonnes)$	4440	0.7012
Longitudinal Center of Gravity (from nose)	$X_{CG}(m)$	32.31	1.761
Vertical Center of Gravity (from keel)	$Z_{CG}(m)$	4.844	0.2856
Vertical Center of Buoyancy (from keel)	$Z_{CB}(m)$	5.644	0.3076
Roll Radius of Gyration	$r_x(m)$	3.433	0.1871
Pitch Radius of Gyration	$r_y(m)$	17.600	0.9592
Yaw Radius of Gyration	$r_z(m)$	17.522	0.9550

Figure 2 shows that the coordinate system applied in this study includes the following two right-handed coordinate systems: the space coordinates system and body-fixed coordinate system, with its origin at the center of gravity on the hull's centerline. The translational and rotational motions in the body-fixed coordinate system are defined by an inertial reference frame in the space coordinates system. Additionally, the x-axis is positive pointing upstream. The y-axis is positive pointing starboard, and the z-axis is positive pointing downward. In the space coordinates system, the coordinates X, Y and Z are used to express the position of the UV coordinate system. Additionally, the orientation of the body-fixed coordinate system is described by the Euler angles ψ (yaw), ϕ (pitch) and θ (roll) as described by Pan [27].

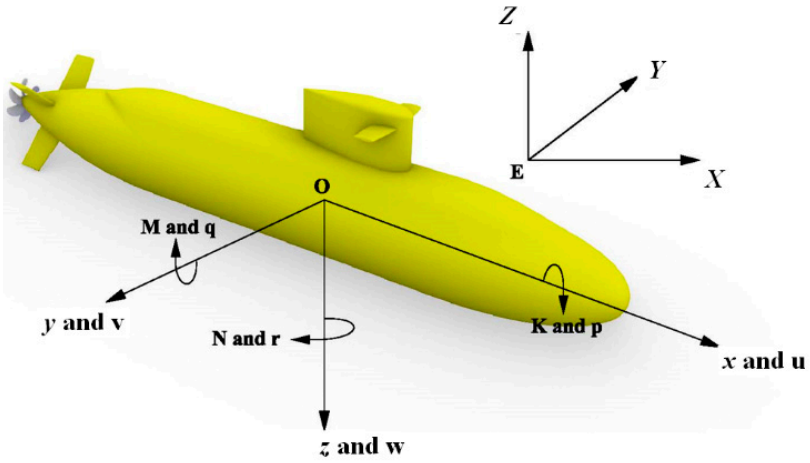

Figure 2. Body fixed coordinate with the origin (O) located at the center of gravity (CG).

2.2. Experimental Details

The experiment was carried out by The Australian Defense Science and Technology Group (DSTG) and the Dutch Defense Materiel Organization (DMO) in 2014 to work together on background research (R&D) on the hydrodynamic behavior of submarines (Overpelt, 2015). The free sailing maneuvering tests were conducted in the Seakeeping and Maneuverings Basin (SMB) in June 2014. The tests included roll decay and kinds of maneuvers in the horizontal plane or the vertical plane, but the downloadable data set does not contain all the maneuvers conducted, and only the roll decay at 0 kn, the horizontal zigzag and turning circle and vertical zigzag are available.

The BB2 model is equipped with X-planes, and all of these four rudders can rotate on their own axis; hence, the deflection of four rudders results in a combined horizontal and

vertical motion. Figure 3 shows the arrangement and the norm direction of the rotation of the X-planes. Throughout the model tests, the submarine was controlled by an autopilot that kept the submarine on course and at depth. The autopilot commanded effective rudder (δ_r) and effective stern plane (δ_s) angles, with individual plane angles (based on the right-hand rule with the thumb pointing away from the body) calculated using the following equations. As there are effectively only two autopilots (horizontal and vertical) some formulas were used to arrive at four individual plane angles:

$$\begin{array}{l} \delta_s = \frac{1}{4}(-\delta_1 + \delta_2 - \delta_3 + \delta_4) \\ \delta_r = \frac{1}{4}(\delta_1 + \delta_2 + \delta_3 + \delta_4) \\ \delta_1 = \delta_r - \delta_s \\ \delta_2 = \delta_r + \delta_s \\ \delta_3 = \delta_r - \delta_s \\ \delta_4 = \delta_r + \delta_s \end{array} \quad (1)$$

where

(1) $\delta_s > 0$, diving rudder, model goes diving and pitch down; $\delta_s < 0$, rising rudder, model goes floating and pitch up.

(2) $\delta_r > 0$, starboard rudder, model turns starboard; $\delta_r < 0$, port rudder, model turns port.

(3) The maximum steering angle for each of the control surfaces is 30 degrees, and the planes go to their commanded angle with their maximum plane velocity of 7.11 deg/s at full scale.

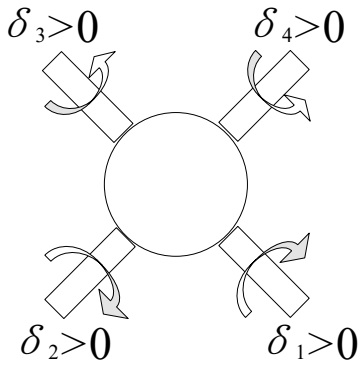

Figure 3. Norm direction of the X-planes.

The attitude control of the model was based on the principle of horizontal and vertical autopilot. A PD (proportional derivative) controller was used to adjust the translation and rotation of the model according to its characteristics during sailing. In practice, for large depth deviation, the translation part was temporarily ignored to prevent the excessive pitch of the model, and the pitch value of vertical motion commands by the PD controller was set to zero degrees.

The parameters of the autopilot used in the control simulation can be obtained according to the scale of the model by a factor of 18.348 (see in Table 2), and the equations for the preset plane angles can be obtained as follows (Kim et al., 2018):

$$\begin{array}{l} \delta_s(t) = P_z e(t) + D_z \frac{de(t)}{dt} + P_\theta e(t) + D_\theta \frac{de(t)}{dt} \\ \delta_r(t) = P_y e(t) + D_y \frac{de(t)}{dt} + P_\varphi e(t) + D_\varphi \frac{de(t)}{dt} \end{array} \quad (2)$$

Additionally, input offset error can be calculated as follows:

$$\begin{array}{l} e(t) = e_{desire} - e_{current} \\ \frac{de(t)}{dt} = \frac{e(t)_{current} - e(t)_{previous}}{t_{current} - t_{previous}} \end{array} \quad (3)$$

where

the subscript "desire" represents the default value of the parameter, the subscript "current" represents the actual value of the parameter, and the subscript "previous" represents the value of the previous time step of the parameter.

For the simulation in this study, it was necessary to control each stern rudder through the steering rate; therefore, the steering rate was set to associate with the planes angle as follows:

$$rudderanglerate[\mathrm{deg}/s] = \frac{\delta_{desire} - \delta_{current}}{\Delta t}, \quad (4)$$

where

δ_{desire} is the preset plane angles based on the PD controller, $\delta_{current}$ is the current plane angles, and Δt is the time step.

Table 2. Autopilot PD parameters for the scaled BB2 submarine by a factor of 18.348.

Description	Proportional Parameter (P)		Derivative Parameter (D)	
	Symbol	Value	Symbol	Value
Translation in y direction (y)	P_y	18.3 [deg/m]	D_y	0 [deg/(m/s)]
Translation in z direction (z)	P_z	−55.04 [deg/m]	D_z	−12.85 [deg/(m/s)]
Rotation about y axis (θ)	P_θ	3 [deg/deg]	D_θ	0.7 [deg/(deg/s)]
Rotation about z axis (φ)	P_φ	3 [deg/deg]	D_φ	2.85 [deg/(deg/s)]

In this study, the straight-line case was chosen and the vehicle speed was 1.2 m/s (10 kn for full scale) (equivalent to a Reynolds number of 5.2×10^6), and the results of the CFD and EFD of the steady turning maneuvers (20 deg to port and starboard) were compared to verify the feasibility and accuracy of the CFD method. In every CFD case, movable control planes in conjunction with a body force propeller using an actuator disk were adopted, and the sailplanes kept no deflection in all CFD maneuvers.

2.3. CFD Method

In this study, the commercial CFD software STAR-CCM+, based on incompressible RANS (the Reynolds averaged Navier–Stokes) simulations, was used to model the flow around the UV and the following RANS equations:

$$\frac{\partial \overline{u}_i}{\partial t} + \overline{u}_j \frac{\partial \overline{u}_i}{\partial x_j} = f_i - \frac{1}{\rho}\frac{\partial \overline{p}}{\partial x_i} + \frac{1}{\rho}\frac{\partial}{\partial x_j}(\mu \frac{\partial \overline{u}_j}{\partial x_j} - \rho \overline{u_i' u_j'}), \quad (5)$$

$$\frac{\partial \overline{u}_i}{\partial x_i} = 0, \quad (6)$$

where $\overline{u}_i$ is the averaged velocity components in the Cartesian coordinates at the meantime, subscript i is the direction in Cartesian coordinates, $\overline{p}$ is the time-averaged pressure, μ is the viscous coefficient, $\rho \overline{u_i' u_j'}$ are the Reynolds stresses, and f_i is the force source term at which a momentum source can be added to simulate flow field. To allow the closure of the time-averaged Navier–Stokes equations, the Reynolds stresses were estimated using various turbulence models. Here, the SST k-ω high Reynolds turbulence model was chosen because of its accuracy and the reliability of the viscous flow around the wall and far-field.

STAR CCM+ is software based on the finite volume method, in which the discretization of the governing equation is carried out on a series of control volumes constituting the computational domain. In this study, the separation flow calculation model was used to separate the velocity term from the pressure term, and the SIMPLE algorithm of prediction–correction was used to solve the flow field. For temporal discretization, the transient term was separated by the second order. The convection term was discretized by the second order upwind, the diffusion term by the central difference scheme, and the gradient using the mixed Gaussian least square method.

2.3.1. Gird

For the direct free sailing maneuvers simulation of UV, the relative motion of each appendage is an inevitable difficulty. For the complex movement of the ship maneuvering system, the rudder planes provide steering force to the hull because of their deflection, and the propeller provides thrust pushing hull sailing due to its rotation. In the meantime, the planes and the propeller move together with the ship's six degrees of freedom. Overset gird can generate meshes of different regions independently and can deal with the relative movement of multiple bodies very flexibly. In the design process, if it is necessary to modify the grid details or add or subtract or replace parts, the overset grid can reduce its difficulty and, for the free sailing of UVs, it has significant advantages; therefore, in this study, the overset grid was adopted to deal with the rudder rotation.

Figure 4 shows the background and the overset regions of the self-propulsion model, with the local refinement on the hull body, appendages and wake region. The wall function was used for the near-wall treatment, and the all-wall y+ wall treatment was carried out for the simulations. The wall spacing was designed to satisfy the condition that the distance to the wall of the first point lies within y+ = 1 for the designed speed, as required by the SST k-ω turbulence mode (Kim et al., 2015; Huang et al., 2017).

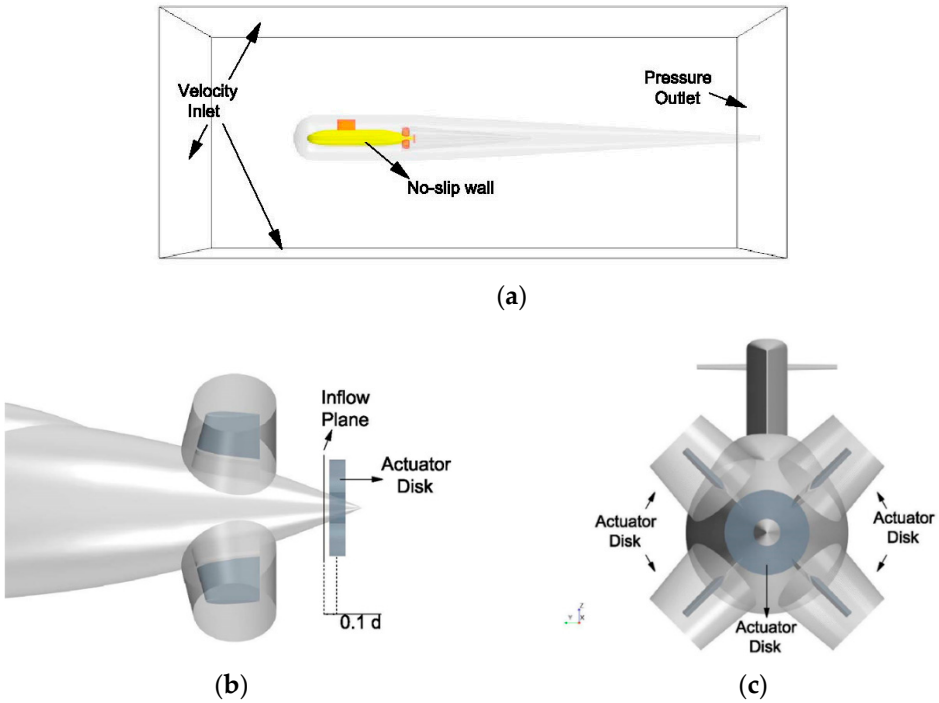

Figure 4. The background and the overset regions containing the control planes: (**a**) Boundary conditions of the computational domain, (**b**) view from the aft and (**c**) magnified view of the stern region showing the positions of the inflow plane.

To ensure the accuracy and quality of interpolation, the mesh size should be kept as consistent as possible around overset grids; if it is not, interpolation may be impossible to achieve. Figure 5 shows the background grid encrypted at the rudder plane's rotation regions; the size of the overset region is the same as that of encryption region.

We noticed that there should be a gap between the rudder planes and the hull body to ensure the deflection of the planes. The gap between the planes and the adjacent surface on the hull was around 1 mm in the physical model. However, the overset interface requires at least three to five layers in the gap (CD-adapco [28], 2021); therefore, the gaps were encrypted to ensure that it had enough mesh.

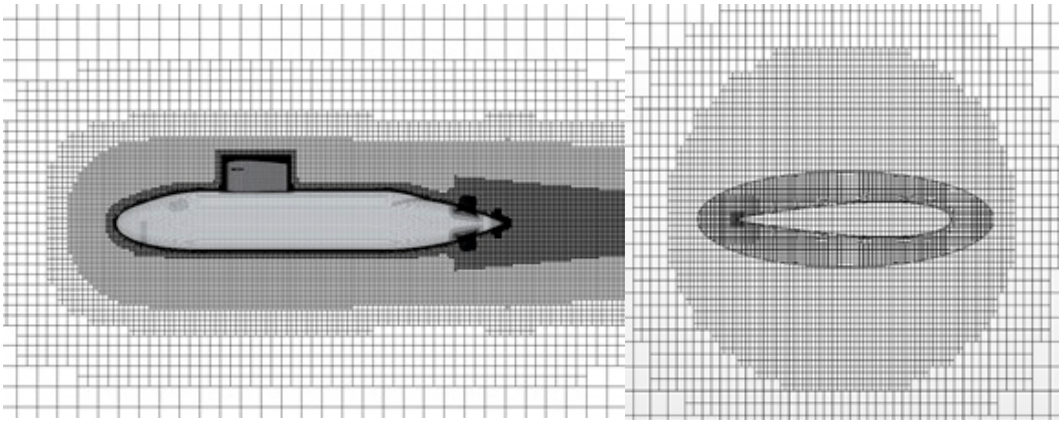

Figure 5. Free-running model grid adopted on y = 0 symmetry plane around the hull body (**left**) and overset grid area of rudder planes area (**right**).

To ensure the convergence of the computational grid, the mesh was encrypted according to the fineness ratio in the ITTC recommendation rules, that is, the mesh was encrypted in three directions by $r_G = \sqrt{2}$, while other parameters remained unchanged (Stern [29]; Zhang [30]). A series of grid levels from coarse to fine are shown in Table 3; the drag force in each case of the towing test is also exhibited.

Table 3. Grid dependence study of the discretized hull and control planes, showing the percentage difference to the fine grid level.

Gird Level	Cells (in Millions)	Drag Force (N)	Difference to Fine (%)
Fine	15.83	24.02	-
Medium	6.58	24.13	0.46
Coarse	2.92	24.50	2.00

The differences of drag forces calculated by medium–fine and coarse–medium is represented by ε_{drag}, then:

$$\varepsilon_{drag1} = F_{medium} - F_{fine}, \quad (7)$$

$$\varepsilon_{drag2} = F_{coarse} - F_{medium}, \quad (8)$$

The changes of ε_{drag} are used to define the convergence ratio R_{drag}:

$$R_{drag} = \varepsilon_{drag1} / \varepsilon_{drag2}, \quad (9)$$

The result of the convergence ratio $R_{drag} = 0.23$, which is in the range of $0 < R_{drag} < 1$. Therefore, the three sets of gird levels are monotonically convergent. For comprehensive consideration, the medium grid configuration (6.58 M cells) was adopted for the self-propulsion simulations in subsequent studies.

2.3.2. Body Force Propeller Model

Normally, viscous numerical methods, such as RANS CFD, detached eddy simulation, and large eddy simulation, have the most potential to capture viscous effects accurately around the propeller. However, when these methods are carried out, the propeller time scale is smaller than the ship time scale, which results in even more costly solutions because the ship must be analyzed with the propeller time scale as Bradford's [31] work. In other words, using the CFD method to simulate the real propeller directly requires a significant amount of time and computing resources; under the circumstances, the body force approach came up (Oda [32]) and was quickly applied to study the disturbance between the propeller and ship body (Kawamura and Miyata [33]; Nakatake [34]; Stern [35]). In research on underwater vehicles, this method has been widely used according to its eligibility in a

study on the ship propeller issue (Phillips [36]; Broglie [37]). Recently, UV's free-sailing and self-propulsion study has adopted it as well (Dubbioso [38]; Sezen [39]; Li [40]). Therefore, in this study, an actuator disk to model the force of the propeller was used to analyze the turning motion ability of a self-propelled submarine. For an overview of the state of the art, the interested reader can be referred to the review conducted in previous work (Huang [3]; Han [41]).

The force source model was used to simulate the influence that the propeller inflicts on the flow, and the body force adopted in this study was uniformly distributed along the axis direction. The propeller used in the simulation was the MARIN 7371R propeller. To obtain the same effect as the real propeller, the characteristics of the propeller should be added into the code. The body force depends on the thrust coefficient K_t and torque coefficient K_q, which can be obtained from the open-water test, and these two coefficients are related to the advance coefficient (J):

$$J = V/nD, \tag{10}$$

where V is the fluid velocity at the propeller location, n is the rotation velocity of the propeller, and D is the diameter of the propeller dish. The open-water curves were obtained from the experimental results in a study conducted by Kim [18], as shown in Figure 6. Illustratively, propeller performance properties were obtained under captive self-propulsion condition, and the advance coefficients (J) were computed based on the average velocities measured at a plane placed 0.136 m in front of the propeller origin; therefore, the propeller coefficients included the wake field influenced by the submarine body and the controller planes, and there was no need to calculate the wake fraction additionally.

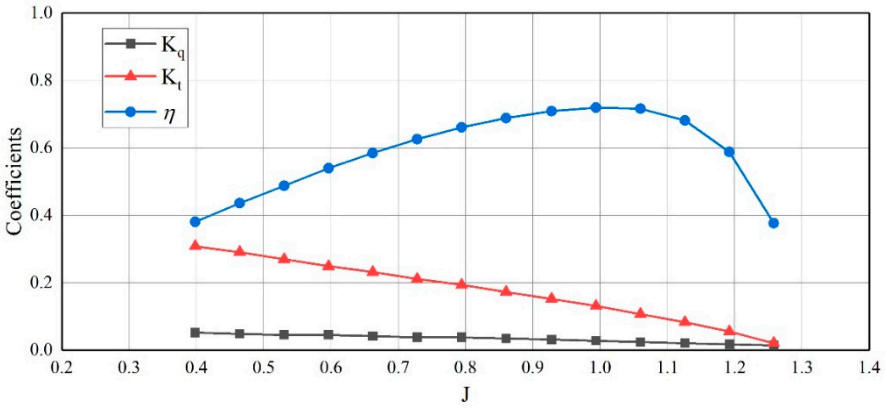

Figure 6. The open-water curves of the MARIN 7371R propeller conducted by Kim.

3. Results and Discussion

All the working conditions of the simulation were set at the same scale as those used in the tank tests, including the hull body, control planes and sail, to ensure that the model and real submarine had similar Froude numbers. Additionally, all the maneuver parameters should be in accordance with certain proportion scaling; the results are shown in Table 4. Pay attention to the fact the test was conducted in fresh water; all the results, ultimately, need to be converted to sea water density.

To ensure the validation, the simulation results need to be translated into a real scale. The results and discussion are divided into two parts, including steady turning maneuvers in deep water and space spiral maneuvers. In the end, this study analyzed the maneuverability and the safety performance comprehensively.

Table 4. Scaling laws (with $\lambda = 18.348$; $\lambda_\rho = \rho_{sea}/\rho_{ba\,\sin}$.

Parameters	Coefficients
Time	$\lambda^{0.5}$
Speed	$\lambda^{0.5}$
Distance	λ
Displacement	λ^3
Moments of inertia	λ^4
Position of CoG	λ
Angular velocity	$\lambda^{-0.5}$
Angular acceleration	λ^{-1}
Force	$\lambda^3\lambda_p$
Moment	$\lambda^4\lambda_p$
Power	$\lambda^{3.5}\lambda_p$

3.1. Straight-Line Maneuver

The turning motion is the most common form of underwater vehicle navigation and is closely related to safety ability. The self-propelled model test is one of the most suitable ways to evaluate the availability and space required for turning maneuvers; it can be the precondition to obtaining the credible results of the six-DOF simulations. The maneuvering simulations usually start from the state of self-propulsion and keep a constant propeller rotation speed after reaching a situation when the propeller thrust is equal to the hull resistance.

In this part, the six-DOF free maneuvering motion of the submarine model in straight-line navigation was carried out based on the numerical simulation results of the early towing tank test. The effects of the propeller are described by the body force model to achieve the thrust and torque on the submarine, and finally, the model reached the target speed of 1.2 m/s, equivalent to about 10 knots in the real-scale submarine. In the process of straight-line sailing, the course is maintained through the autopilot system, and the depth and pitch are kept by vertical control commands; the commands in this study were 0. A noteworthy point is that the experimental data employed for validation used stern and sailplanes for vertical control, while the CFD simulations only used stern planes for vertical control because of the limited availability of experimental data. We speculate that the experimental data were still deemed to be acceptable for the validation of the CFD prediction because both the sail and stern planes are mainly used to maintain the vertical position for a straight-line course, and one of their effects may be enough. The results show that the vertical (pitching angle) control is very good. The results of CFD simulations and tests are shown in Table 5.

Table 5. Result of CFD simulations and tests (all results are at full scale).

Parameters	CFD	EFD	Error (%)
Vehicle Speed (kn)	10.2	10	2.00
Propeller Revolution (rpm)	272	266	2.26
Thrust Force ($N{\cdot}10^5$)	1.61	1.63	1.23
Pitch Angle (deg)	0.89	0.92	−3.26
Vertical Position ($/L_{PP}$)	0.02	0	-

Figure 7 shows the vortex structure diagram of the submarine model. The wake area of the propeller is shown as a circle, which is also the part where the vortex structure of the body force model is different from that of the discrete propeller. Meanwhile, the horseshoe vortices caused by the shell, tip vortex and hub vortex can be seen in the figure as well.

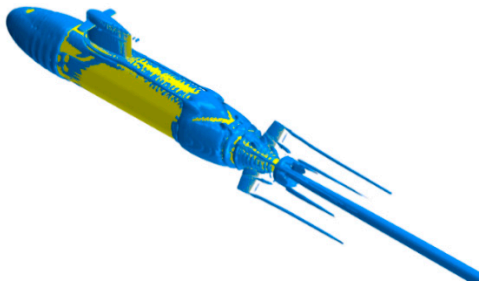

Figure 7. Vortical structures shown as isosurfaces.

3.2. Steady Turning Maneuver

Steady turning maneuvers include turning to the portside and the starboard side on the horizontal plane at a rudder angle of ±20 deg. The submarine model starts direct flight at a target speed of 1.2 m/s (10 kn for full scale). When it reaches this, it keeps the propeller speed constant and sets the turning rudder angle to ±20 deg. After that, the submarine model starts to turn. The heave and pitch of the submarine model are controlled by the autopilot, which noticed that the shell planes maintain 0 deg in the whole process. The related data and icons are converted into real-scale data through scale ratio and compared with the results of the tank test.

Table 6 shows the difference between the test and CFD turning motion parameter results, and the results are dimensionless according to the requirements of ITTC [42]. Figure 8 shows the comparison of the left and right rudder trajectories predicted by CFD with the test results and Carrica's results shown in the graph as well. The comparison only includes the tactical diameter and longitudinal distance in the test and CFD prediction, since the test did not perform a complete turning operation. The results show that the trajectory obtained by the CFD numerical prediction is in good agreement with the test results. While the error between the 180° turning time of the left turn is 10.19%, the other turning motion parameters can be within 10%. The CFD simulation in this study can better predict the free sailing maneuver characteristics of the submarine and provides an effective pre-evaluation method for evaluating the maneuverability of the submarine.

Table 6. Percentage difference between CFD and experiment (from Overpelt's reports)/study results for length (L)-based non-dimensional maneuvering characteristics (ITTC [42], 2002) for effective rudder angles 20 deg and −20 deg steady turning maneuvers.

Effective Rudder Angle		Turning Diam (/L)	Transfer (/L)	Tactical Diam (/L)	Advace (/L)	90° Turning Time (s)	180° Turning Time
−20 deg PT	CFD	2.89	1.45	3.13	2.53	47.8	93.4
	EFD	-	1.55	3.24	2.65	52.6	104.0
	Difference (%)	-	−6.45	−3.39	−4.91	−9.12	−10.19
20 deg SB	CFD	2.91	1.50	3.15	2.50	49.8	101.9
	EFD	-	1.63	3.33	2.61	54.1	106.2
	Difference (%)	-	−7.97	−5.41	−4.21	−7.95	−9.25

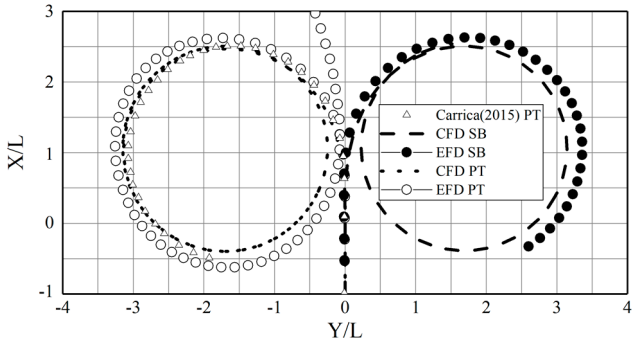

Figure 8. *X-Y* trajectories for steady turning maneuvers at a forward speed of 1.2 m/s.

Turning diameter: diameters of the circular arc traveled by the CG at a vehicle's heading angle of 180°.

Transfer: perpendicular distance traveled by the CG at a vehicle's heading angle of 90°.

Tactical diameter: perpendicular distance traveled by the CG at a vehicle's heading angle of 180°.

Advance: distance traveled by the center of gravity (CG) in a direction parallel to the original course at a vehicle's heading angle of 90°.

Figure 9 shows the time history curve of the pitch angle and roll angle. The results show that the submarine presents a slightly bow-down posture during the straight-line sailing. During the turning maneuver's progress, the submarine is affected by the hydrodynamic force and affected by a bow-up moment, and the steady-turning submarine reaches and finally maintains a stable bow-up angle. This may be due to the external force generated by the control plane surfaces, resulting in a downward force around the tail of the submarine (Leong et al., 2016 [43]). The prediction results also reflect that the results of the left and right rudder rotation pitch angles predicted by CFD are about 0.7 deg greater than the test results, but because the CFD results are more inclined to the bow during the straight flight stage, the test results are based on the net change in the pitch angle, which shows good agreement with the CFD forecast results. In the process of the turning motion, the model tends to fall in, which is consistent with the general regular submarine's rolling rule. The changing rate of the roll angle predicted by CFD at the beginning of the turning motion is basically the same as the test results; gradually and in the end, the value seems to be larger than that of the test. Since the CFD simulation is based on the six-DOF maneuvering motion, there is a certain coupling relationship between the pitch angle and the roll angle; therefore, the prediction error of the pitch angle also affects the prediction result of the roll angle.

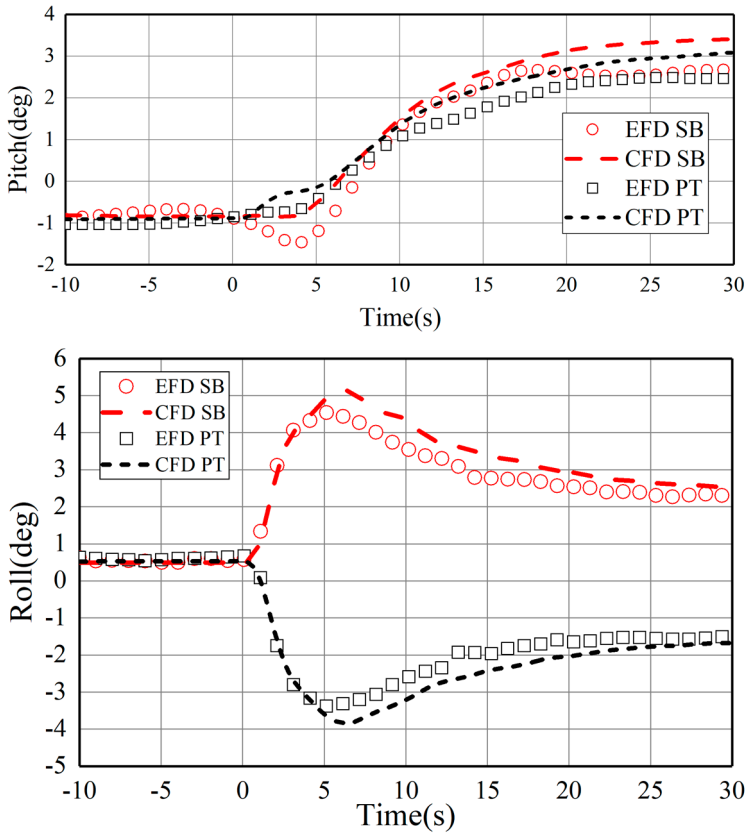

Figure 9. Time histories of pitch (**top**) and roll (**bottom**) for the 20 deg controlled turn maneuvers.

Figure 10 shows the time history curve of the depth change. The results show that at the beginning of the turning motion, the depth predicted by CFD is above the initial position, and there is a certain error, which is caused by the slight difference between the center of gravity position of the CFD model and the test model. Meanwhile, there is a gap between the control plane and the hull body when using overset grids to achieve the deflection; we chose to cut part of the model volume, which, to a certain extent, caused an error in the submarine model weight and the test value, and finally may have caused the submarine model to be generated. The rising force causes the submarine to be higher than its initial depth during straight-line sailing. However, during steady turning, the depth changes of the CFD prediction results and the test results gradually decrease and finally converge to a fixed value, showing good consistency.

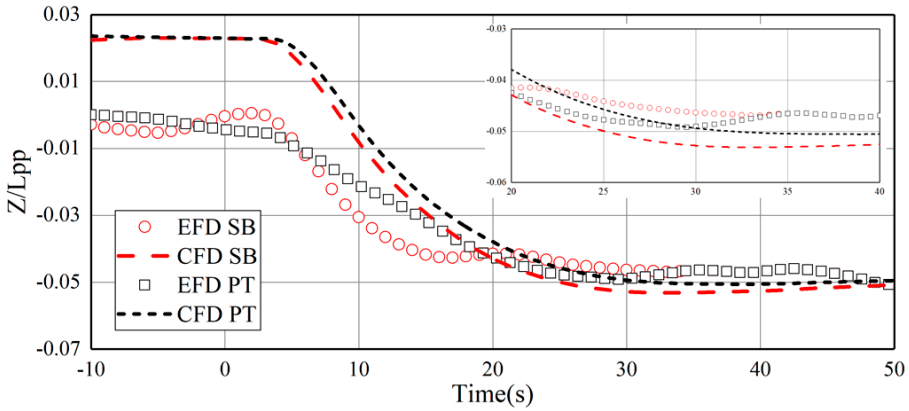

Figure 10. Time histories of depth changes for the 20 deg controlled turn maneuvers.

The change curve of the submarine speed is shown in Figure 11. The results show that CFD can predict the speed reduction in the model in good agreement with the experimental results. It can be seen from the figure that the right turn speed of the CFD has further decreased, from about 10 knots to less than 6 knots. This phenomenon indicates that the submarine received more resistance when turning to starboard. Figure 9 shows that the submarine presents a greater bow lift when turning right, which also causes greater resistance in the sailing direction and make the model slower.

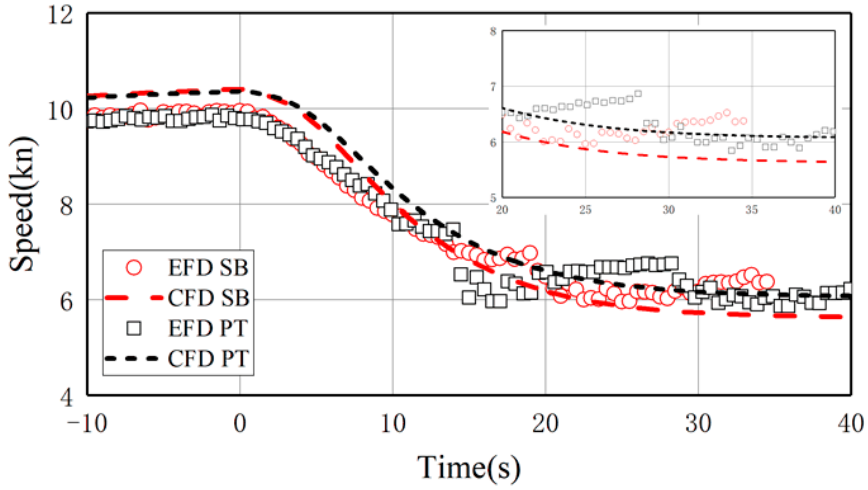

Figure 11. Evolution of speed for the turn maneuvers.

Figure 12 shows the evolution of the yaw rate. The results show that the changing trend of the yaw rate is slightly over-predicted by CFD but totally consistent with the experimental results during the steady turning process. The yaw rate gradually decreases

and converges to a stable result and is larger than those of the test, both in portside and starboard side turning, which leads to a better turning performance. It is interesting that CFD predicts the speed drop in the turning process well. Figure 11 shows that the speed drop is basically the same as the test results, which means that at the same speed, the turning trajectory predicted by CFD will be more compact, that is, the turning circle will be smaller. This is also consistent with the results shown in Figure 8.

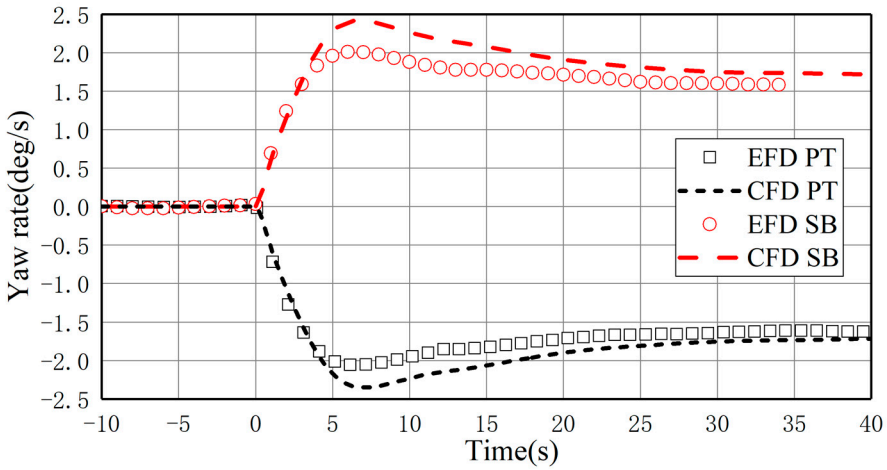

Figure 12. Evolution of yaw rate for the turn maneuvers.

The propeller thrust results are shown in Figure 13; when the model starts turning, the thrust of the propeller drops significantly. The test thrust drops by up to one-third, while the CFD-predicted drop is only about 12%, which may be because of the heavy attack on the stern's surface. The body force propeller used in the software uses an approximate model to replace the real propeller, ignoring the effects of blades and gaps; thus, the captured incoming flow cannot completely simulate the real flow field. When the speed is reduced from 10 to 6 knots, that is, after entering stable turning, the thrust is increased by about 14% compared with the direct flight state. The CFD prediction results are in good agreement with the test results. At the same time, the propeller thrust is well predicted when turning to the starboard side. At the beginning of the turning, the yaw rate and the transverse velocity increase rapidly, as shown in Figure 12; thus, the inflow in front of the propeller plane increase as well and may be larger than the velocity of the vehicle, and the influence of the yaw rate and transverse velocity makes the freestream velocity increase while the vehicle speed decreases. Thus, the axial velocity of the propeller increases, and $u_{propeller} > u_{vehicle}$ as a result. Additionally, with the turning motion continuing, the influence of the decrease of vehicle speed dominates, and the thrust begins to increase, which can be proved by the curves of yaw rate, since the yaw rates are basically constant after t = 10 s.

Figure 14 shows some interesting characteristics of the flow field. The tip vortices generated by the right plane of the shell are captured by the tip vortices generated because of the separation of the shell tip, and only the tip vortices of the shell are left afterward. The horseshoe vortices generated at the roots area of the stern planes are all clearly visible. The secondary vortices in the hull area intersect with the horseshoe vortex generated by the right downside plane, cause a low-pressure area above the entire right side of the model and work together with the other three planes to make the model drift and turn. The separation vortex is then captured by the propeller wake, fused with the unique wake vortex of the body force propeller and deformed.

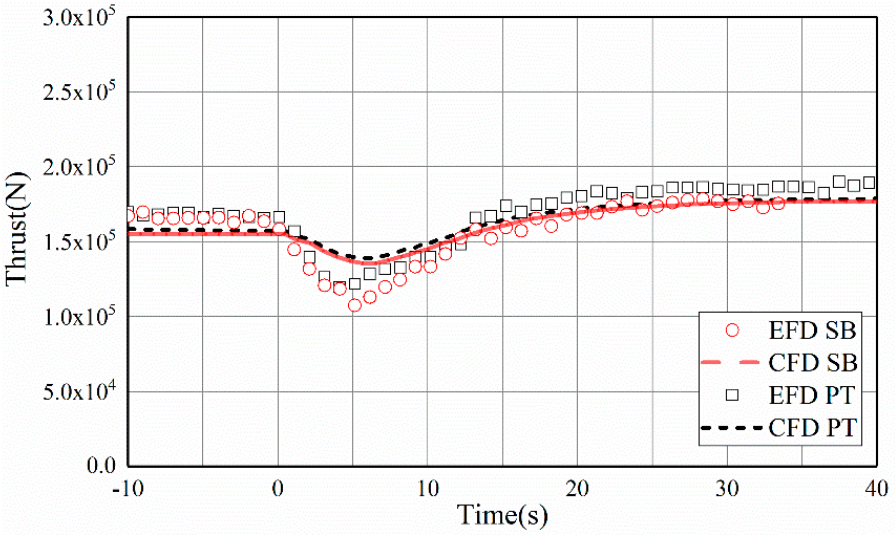

Figure 13. Evolution of propeller thrust forces for the turn maneuvers.

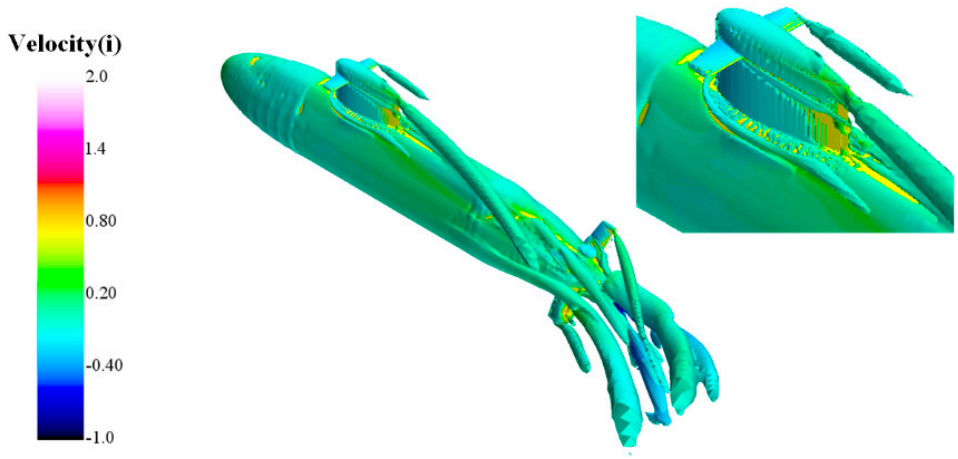

Figure 14. Vortex view of the -20 deg controlled turn maneuver at t = 50 s.

In summary, the six-DOF CFD prediction is consistent with the test results, the simulation of turning motion has good accuracy and the control effect of the autopilot on the depth and posture of the submarine is also good. Ideally, the same numerical method will be used to predict the space spiral maneuvering of the submarine in subsequent studies.

3.3. Space Spiral Maneuver

When the submarine is diving and floating underwater to achieve the tactical goal of changing depth, it may maneuver with a turning motion to avoid attacks or just to ensure the comfort of the crew. The space spiral maneuver is the most common, and normally the submarine deflects its rudders and stern-planes to a predetermined degree—sometimes it only needs its rudders—and the submarine gradually moves into space and spirals. In the simulation, the vertical command is sent by the autopilot, and at the beginning of the CFD prediction, the submarine self-propelled and sailed directly into deep water at a speed of 1.2 m/s (10 kn for full scale). At t = 0 s, the effective rudders rotate $\pm$20 deg, and at the same time, the vertical command is set to $\pm$8 deg for the autopilot. The 3D trajectory prediction diagram is shown in Figure 15. It is worth noting that the results show some interesting phenomena, which indicates that the submarine is in an underwater space. It has more complex maneuverability and combat performance during movement.

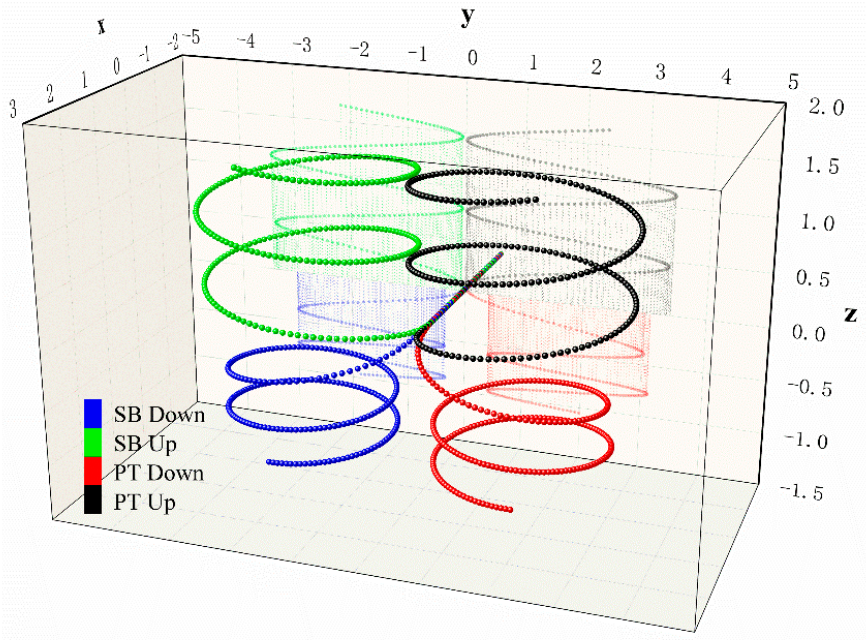

Figure 15. 3D trajectories for the space spiral maneuvers.

Figure 16 shows the *X*–*Y* projections of the spiral trajectory under the four cases. The figure shows some unexpected results: the upward and downward spiral circles show larger differences. The trajectory parameters are shown in Table 7. The trends of the left and turn trajectory curves are relatively close in combination with Figure 16. However, it is worth noting that when the submarine reaches the starboard steady spiral maneuver, it deviates further from the original line, with a first heading change of 180 deg. From this point of view, the port spiral maneuver shows a better turning ability. Another noteworthy phenomenon is that the predicted longitudinal distance is larger when rising, which causes the trajectory of the rising maneuver to overpass the initial position. Thus, it must ask for more space to complete the spiral rising maneuvers, which indicates that the submarine has a better flowing performance when submerged.

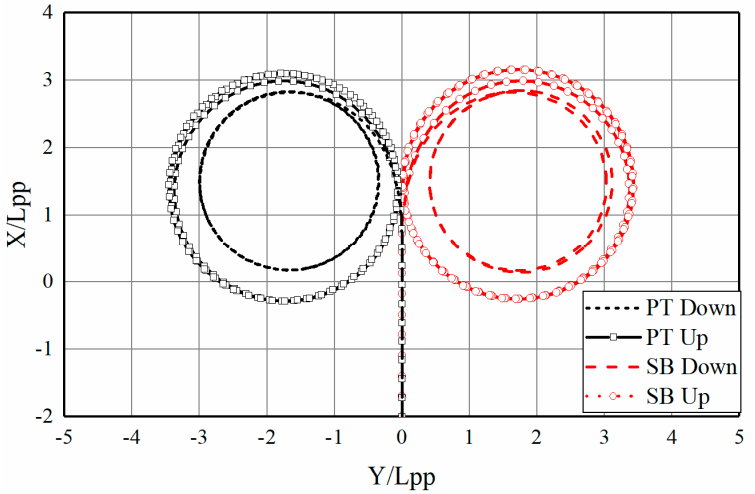

Figure 16. *X*–*Y* trajectories for the space spiral maneuvers.

Table 7. Parameters for effective rudder angles 20 deg and −20 deg space spiral maneuvers.

Parameters	−20 deg Turn to Port		20 deg Turn to Starboard	
	Rising	Submergence	Rising	Submergence
Turning diam/Lpp	3.42	2.64	3.41	2.69
Tactical diam/Lpp	3.39	3.00	3.36	3.03
Longitudinal distance/Lpp	3.00	2.85	2.99	2.81
Positive constant distance/Lpp	1.78	1.65	1.75	1.61

Figure 17 shows the time history curve of the pitch and speed. The speed of the submarine decreases and gradually converges to a stable value. According to the CFD prediction, the speed drops by about 30% when rising, while it drops by 45% when submerged. The turning diameter of a submarine is related to the speed and the efficiency of the rudder angle. The diameter of the rising maneuver will surely be larger because of the higher speed with the efficient rudder deflection angle of 20 deg, which is consistent with the *X*–*Y* plane projection of the CFD prediction. The yaw rates are also shown in Figure 17, which experienced an increased peak, and then decreased and converged to a stable result. The results of the portside and starboard side maneuvers show good consistency, while the rising results are a little bit larger than those while submerged. In general, the turning abilities of the space spiral maneuvers show little difference while rising and submerged; in other words, the effect of an efficient rudder is on the same level, and thus the ability to follow is hardly influenced by vertical control or the deflection of efficient stern planes. Based on the CFD prediction in Figure 16, a larger speed means a larger turning diameter, while a similar yaw rate, that is, the turning ability of submergence, appears to be better.

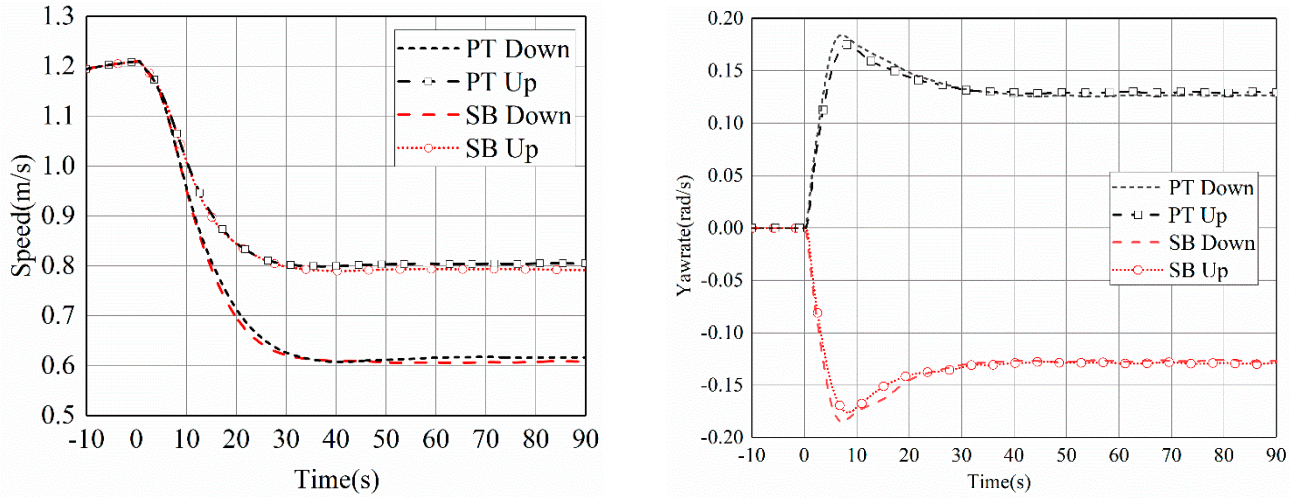

(**a**) (**b**)

Figure 17. Evolution of speed (**a**) and yaw rate (**b**) for the space spiral maneuvers.

Figure 18 shows the evolution of the pitch angle and roll angle. The roll angle first quickly increases to a peak and then gradually converges to a stable result. The peak value of rising (about 3 deg) is smaller than submergence (about 4 deg). From when the planes finish rotating (about 1 s) until the model is under the steady spiral maneuvers (about 30 s), that is, the moment when the parameters just stop changing, the model is affected by resistance, and the speed is significantly reduced. Additionally, at the same time, there is a lateral moment that acts on the center of gravity and makes the model rotate and fall in. The results show a larger roll angle of submergence, which indicates worse safety. When the drag torque, lateral moment and control plane torque are balanced, the model achieves steady spiral motion, and the results suggest a stable roll angle with little difference in the four cases.

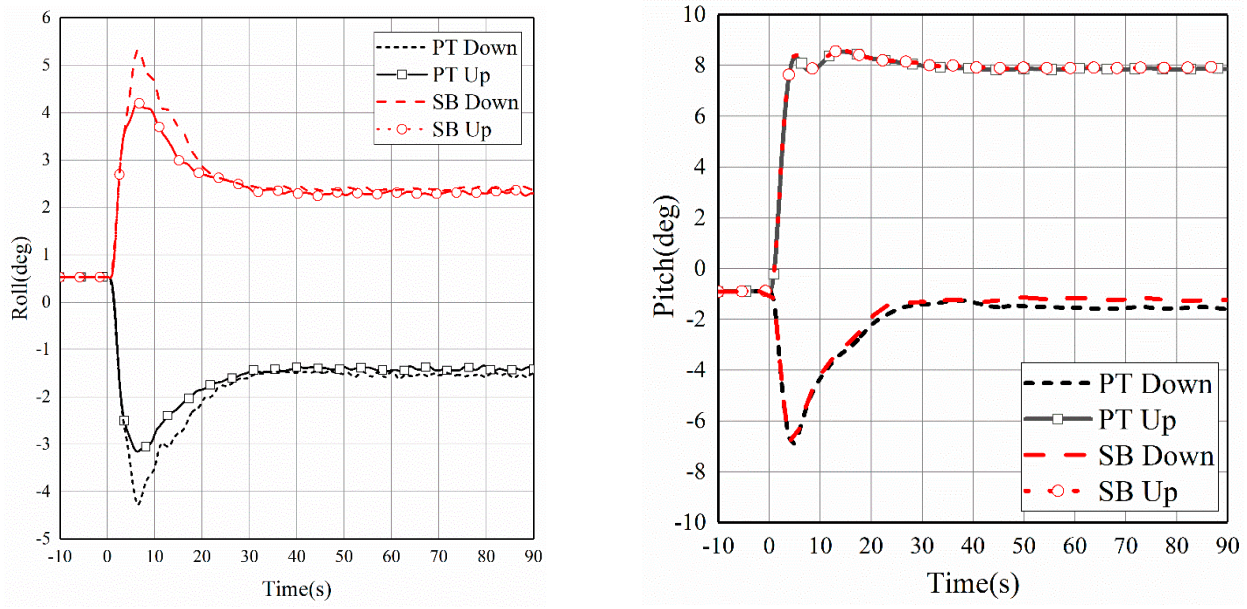

(**a**) (**b**)

Figure 18. Evolution of roll (**a**) and pitch (**b**) for the space spiral maneuvers.

The result of the pitch angle presents an interesting phenomenon; vertical commands of 8 deg and −8 deg set in the autopilot at t = 0 s make the model maneuver the bow up and bow down. The pitch angle prediction of rising fluctuates several times and finally converges, maintaining slightly less than 8 deg. However, the prediction of submergence seemed to realize the command was impossible; the result shows that the pitch angle reaches the peak (about −7 deg) quickly and then, as the speed decreases, it gradually converges, maintaining about −1 deg for spiral submerging. When the submarine is turning underwater, the pressure difference caused by the speed drop works with the resistance t caused by the internal roll to cause an objective sinking force behind the shell. From the effect of force, the deflection of the model shows there must be a pitch moment that causes the body to bow up to oppose the moment of stern planes during turning underwater.

Figure 19 shows the projection of trajectory on the X–Z plane and the evolution of the depth. The curves of submergence seem to be sharper than the rising curves, and the results of the two depth changes are closer between portside and starboard side turning, while the change trend of the submergence maneuver is gentler. Generally, the change of depth while the model heading is 360 deg is defined as the lift distance, $\Delta\zeta$. According to the CFD prediction, the lift distance for the portside and the starboard side turning is 0.66 and 0.65 while rising, and −0.36 and −0.33 during submergence, respectively. From the results, when the model submerges, part of the bow-down moment caused by the stern planes is balanced by the bow-up hydrodynamic moment that reduces the submarine's pitch angle and slows the tendency to submerge.

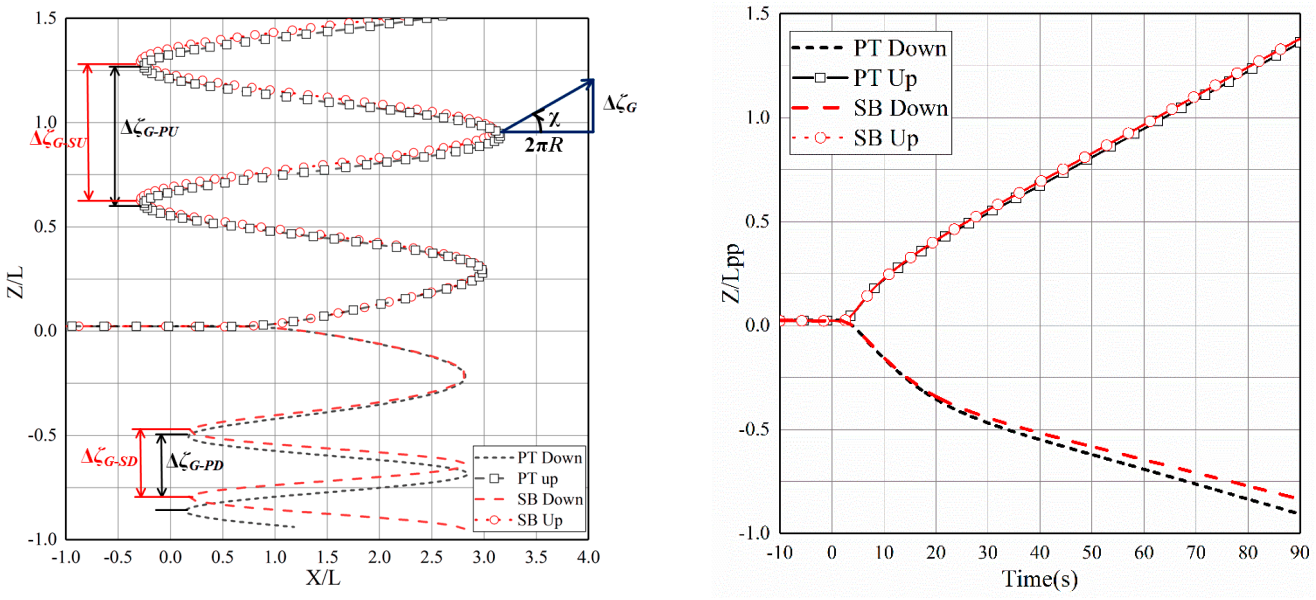

(**a**) (**b**)

Figure 19. *X*–*Z* trajectories (**a**) and evolution of depth (**b**) for the space spiral maneuvers.

The evolution of the controller plane deflections, the forces at the Z–axis and the pitch moments of the portside turning spiral maneuver are shown in Figure 20. The (a) and (b) are actually the defections of the effective rudder and effective stern plane. The defections follow the commands of autopilots (PD controllers), and if the controller wants the vehicle to sail with pitch angle while turning, two commands are given: the horizontal angle is maintained by effective rudders, and the vertical motion (pitch angle) relies on the autopilot commands (transferred to effective stern planes). When the model rises, the autopilot input commands the model to bow up to 8 deg and the stern-plane deflection is more than 25 deg at the beginning. After the command is completed, the deflection decreases rapidly and is finally approximately equal to 0. However, the autopilot command does not seem to be well satisfied when the model submerges. The stern plane deflection is almost −20 deg during the whole spiral maneuver, which forces the model to pitch to −2 deg, rather than −8 deg, according to Figure 18. The comparisons of force and moment show that the submarine has the characteristic of "stern heavier" during the spiral maneuver; the model's body is subjected to a bow-up moment while rising but is almost 0 while submerging, which means the moment of the sinking force balances the moment of the stern planes, that is, when the model is rising, these two moments are in the same direction and work together to make the model bow-up, and the autopilot only needs a small vertical command to make the stern planes deflect.

Figure 21 shows the surface pressure of the model body at t = 90 s. At this moment, the hull shows bow-up (a) and bow-down (b) motions. In general, during the turning motion, the flow field around the body changes, and the phenomenon "sidewash" shows up, which creates a pressure difference between the top and bottom of the model. The high-pressure areas are located around the shell, while the low-pressure areas are located at the tail zone and the forepart of the control planes at the top of the body; the pressure difference between these regions forms the sinking force. A distinct low-pressure area appears at the rear of the bottom, producing a bow-up moment, which is balanced with the stern planes moment and the sinking moment when turning. At the same time, an obvious pressure gradient appears from the starboard side to the port side of the hull, forming a lateral force pointing to the left side of the model, providing a turning moment for portside turning. A comprehensive comparison shows that the peaks in the high-pressure zone and low-pressure zone are higher during the rising maneuver, which also shows that the submarine receives a larger pitching moment and results in a larger pitch angle when rising.

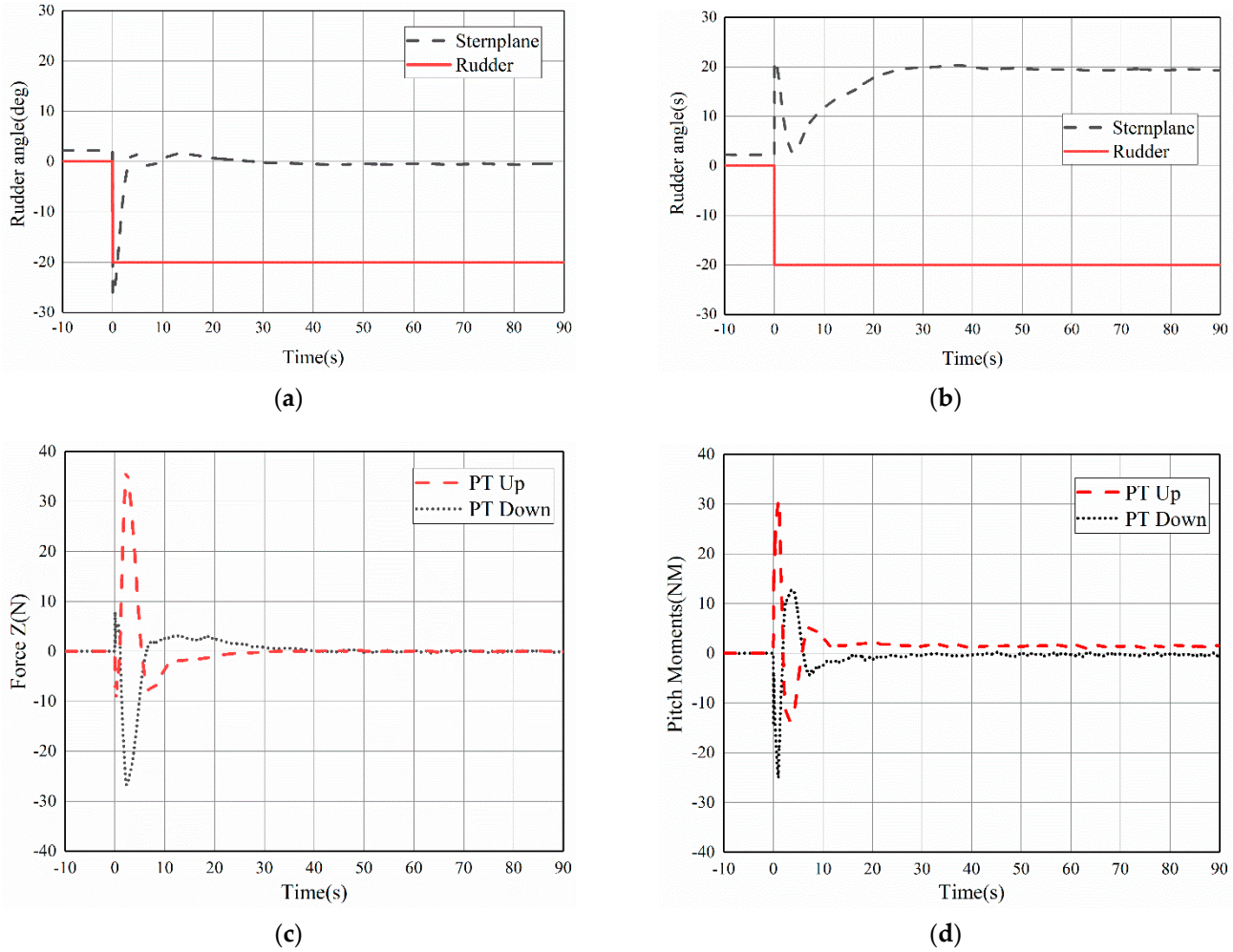

Figure 20. Evolution of the controller plane deflections (**a**,**b**), forces at Z-axis (**c**) and pitch moments (**d**) for the left turning space spiral maneuvers.

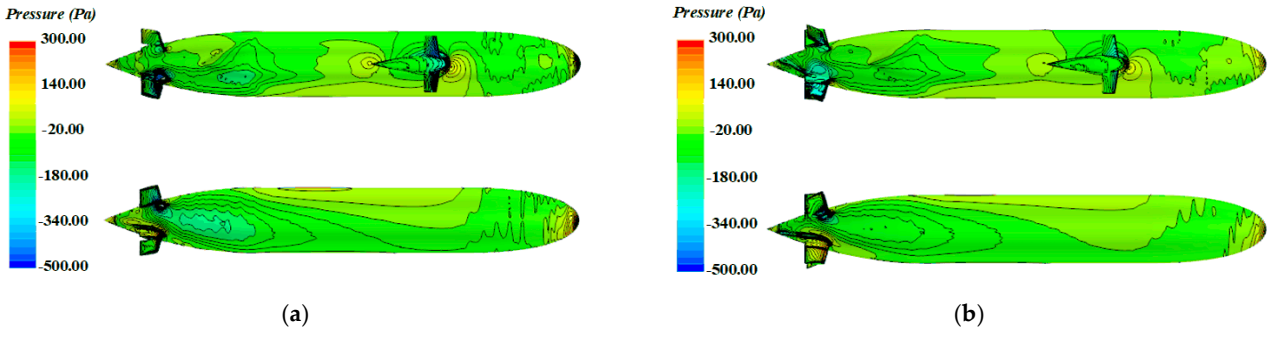

Figure 21. Top and bottom surface pressure of rising (**a**) and submergence (**b**) for the left–turning space spiral maneuvers.

Figure 22 shows a vortex near the model's body during the steady spiral maneuvers. The vortex structure on the leeward side is obvious as well as the separation phenomenon around the body's surface when the hull is in the side wash. There are several tip vortices formed by the shell and its upper tip, and at the bottom of the shell, the horseshoe vortex extension merges with the hull vortex and is transported to the propeller area. At the same time, the chain vortex formed by the control planes is also merged with the body vortex at the stern, as well as the unique circular vortex that belongs to the body force propeller and the secondary vortex, which makes the flow more complicated at the stern zone. The phenomenon in the figure also shows that the vortex near the stern of submergence

separates more thoroughly; however, the speed of flow seems to be smaller than it was during the rising maneuver. It can be seen also in Figure 17 that the speed drop is larger during submergence, as the separation surely interferes with the inflow of the propeller and has a negative effect on the maneuverability of the submarine.

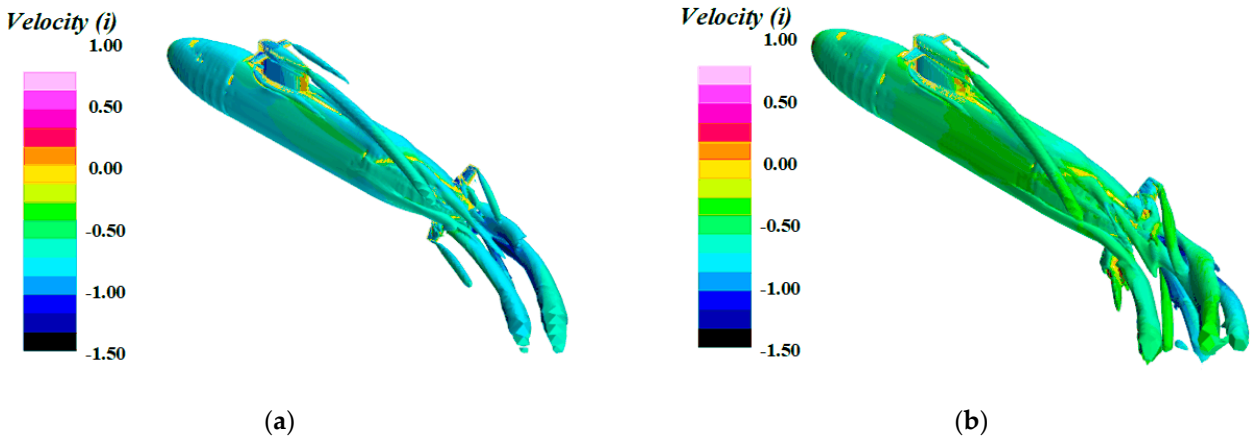

Figure 22. Vortex of rising (**a**) and submergence (**b**) for the left–turning space spiral maneuvers.

3.4. Results Discussion

The simulations of our work are divided into three parts, including straight-line maneuvers, steady turning maneuvers in deep water and space spiral maneuvers. The settings were based on the experiments, and a body force model was used to simulate the effects of the propeller. All the planes can rotate within their own axis, and their deflections were commanded by horizontal and vertical autopilots, which were normal PD controllers with a combined proportional and differential control parameter for translations and rotations. The comparison about straight-line maneuvers and steady turning maneuvers of CFD and experiments showed the vertical (pitch angle) control is very good, and the submarine could reach the target speed of 1.2 m/s, equivalent to about 10 knots in the real-scale submarine.

In the simulations of space spiral maneuvers, we conducted scenarios for diving and floating as well as the turn to portside and starboard. The vertical commands in this manuscript are 8 deg and −8 deg. The results are very interesting, and the submarine showed the phenomenon of "stern heavier" when turning underwater. The flow fields around the sail and the flow fields between the top and bottom all changed when the vehicle turned. The side wash appeared as a result; thus, the speed difference appeared in these zones. Based on Bernoulli's equations, the difference in speed caused a difference in pressure between the top and bottom—the bow and stern—which was also the reason the vehicle rolled to the inside. The vertical component of the resistance acting on the bow was larger than that acting on the stern, so there would be a considerable vertical force point at the bottom, behind the sail, and so the vehicle appeared to bow up.

4. Conclusions

In this study, the CFD method was used to predict the underwater turning ability of the general submarine model BB2, including steady turning maneuvers and space spiral maneuvers. The overset mesh was carried out to deal with the relative multibody motion, and the variations in the free sailing trajectories and hydrodynamic loads were analyzed in a Reynolds-averaged Navier–Stokes (RANS) simulation with the assumption of a body force propeller model to ensure it was self-propelled. The numerical prediction also included the dynamic deflection of the control planes, where the deflection angle command is issued by the autopilot. The numerical prediction of the characteristic parameters of the turning maneuvers agreed well with the results of a tank test, and the CFD method used in this study can accurately simulate self-propelled tests and is therefore is a cost-effective tool that

can replace more expensive self-propelled tests. The prediction of the six-DOF maneuvers enables designers to determine the maneuverability and safety of the submarine and help with the research on and design of the underwater vehicle.

Space spiral maneuvers are predicted based on the horizontal turning, and the attitude is controlled by the autopilot. The predicted results of rising maneuvers are in line with expectations, and the pitch angle is within 3% of the preset value of the final steady spiral maneuvers. However, the submergence maneuvers have not performed as well as expected, and the vertical and horizontal motions of the submarine under six-DOF show strong mutual interference effects. Through the analysis, the turning motion was found to have a greater impact on the depth and pitch, and the effective rudders' deflection makes the submarine appear to be "stern heavier". This prediction shows that, even if the vertical command is over 20 deg, the pitch angle eventually remains below 2 deg of the submergence maneuvers. The "stern heavier" and motion characteristics when turning underwater might help to save the submarine in a situation of dangerous submergence, as the turning motion can be an effective way not only to reduce the speed but also to limit the dangerous depth, which plays a role in correlational research between safety and maneuverability.

The work in this article made certain reference to the CFD prediction of the maneuverability of an underwater vehicle and evaluated the research on a dangerous situation. Since the current CFD simulation only considered the space turning performance and the stability of roll, further design and research on repeated steering is needed.

Author Contributions: Conceptualization, K.H., X.C., Z.L. and C.H.; methodology, K.H., X.C., Z.L. and C.H.; software: K.H. and K.T.; validation: K.H., H.C. and J.Y.; formal analysis: K.H. and X.C.; data curation: K.H., H.C. and J.Y. All authors have read and agreed to the published version of the manuscript.

Funding: This research was funded by the National Natural Science Foundation of China [grant numbers 551720105011, 51979211], Key Research and Development Plan of Hubei Province(2021BID008), Research on the Intelligentized Design Technology for Hull Form. Green Intelligent Inland Ship Innovation Programme. High-tech ship research project (2019[357]).

Data Availability Statement: The data presented in this study are available in this article (Tables and Figures).

Conflicts of Interest: The authors declare no conflict of interest.

References

1. Gertler, M.; Hagen, G.R. Standard Equations of Motion for Submarine Simulation. (NSRDC-2510). *Engineering* **1967**. [CrossRef]
2. Feldman, J. DTNSRDC Revised Standard Submarine Equations of Motion. 1979. Available online: https://ntrl.ntis.gov/NTRL/dashboard/searchResults/titleDetail/ADA071804.xhtml (accessed on 1 November 2021).
3. Huang, C. Direct Simulation of Maneuver of the Underwater Vehicle Based on Overset Grid. Master's Thesis, Wuhan University of Technology, Wuhan, China, 2018.
4. Bettle, M. Unsteady Computational Fluid Dynamics Simulations of Six Degrees-of-Freedom Submarine Manoeuvres. Ph.D. Thesis, University of New Brunswick, Fredericton, NB, Canada, 2013.
5. Itard, X. Recovery procedure in case of flooding. In Proceedings of the Warship International Symposium Conference, Brisbane, Australia, 22–25 August 1999.
6. Issac, M.T.; Adams, S.; He, M.; Bose, N.; Williams, C.D.; Bachmayer, R.; Crees, T. Manoeuvring experiments using the MUN Explorer AUV. In Proceedings of the 2007 Symposium on Underwater Technology and Workshop on Scientific Use of Submarine Cables and Related Technologies, Tokyo, Japan, 17–20 April 2007.
7. Jun, B.; Park, J.; Lee, F.; Lee, P.; Lee, C.; Kim, K.; Oh, J. Development of the AUV 'ISiMI' and a free running test in an ocean engineering basin. *Ocean Eng.* **2009**, *36*, 2–14. [CrossRef]
8. Toxopeus, S.; Atsavapranee, P.; Wolf, E.; Daum, S.; Pattenden, R.; Widjaja, R.; Zhang, J.T.; Gerber, A. Collaborative CFD exercise for a submarine in a steady turn. In Proceedings of the International Conference on Offshore Mechanics and Arctic Engineering, Rio de Janeiro, Brazil, 1–6 July 2012; pp. 761–772.
9. Quick, H.; Woodyatt, B. Experimental Testing of a Generic Submarine Model in the DSTO Low Speed Wind Tunnel. Phase 2. Defence Science and Technology Organisation Fishermans Bend (Australia) Aerospace Div. 2014. Available online: https://citeseerx.ist.psu.edu/viewdoc/download?doi=10.1.1.915.6230&rep=rep1&type=pdf (accessed on 1 November 2021).

10. Chase, N. Simulations of the DARPA Suboff Submarine Including Self-propulsion with the E1619 Propeller. Master's Thesis, University of Iowa, Iowa, IA, USA, 2012.
11. Groves, N.C.; Huang, T.T.; Chang, M.S. Geometric characteristics of DARPA (Defense Advanced Research Projects Agency) SUBOFF Models (DTRC Model Numbers 5470 and 5471). David Taylor Research Center Bethesda MD Ship Hydromechanics Dept. 1989. Available online: https://www.researchgate.net/publication/235092809_Geometric_Characteristics_of_DARPA_Defense_Advanced_Research_Projects_Agency_SUBOFF_Models_DTRC_Model_Numbers_5470_and_5471 (accessed on 1 November 2021).
12. Chase, N.; Michael, T.; Carrica, P.M. Overset simulation of a submarine and propeller in towed, self-propelled and maneuvering conditions. *Int. Shipbuild. Prog.* **2013**, *60*, 171–205.
13. Broglia, R.; Dubbioso, G.; Durante, D.; Di Mascio, A. Turning ability analysis of a fully appended twin screw vessel by CFD. Part I: Single rudder configuration. *Ocean Eng.* **2015**, *105*, 275–286. [CrossRef]
14. Dubbioso, G.; Broglia, R.; Zaghi, S. CFD analysis of turning abilities of a submarine model. *Ocean Eng.* **2017**, *129*, 459–479. [CrossRef]
15. Feng, D.; Chen, X.; Liu, H.; Zhang, Z.; Wang, X. Comparisons of Turning Abilities of Submarine with Different Rudder Configurations. In Proceedings of the ASME 2018 37th International Conference on Ocean, Offshore and Arctic Engineering, Madrid, Spain, 17–22 June 2018.
16. Yasemin, A.O.; Munir, C.O.; Ersin, D.; Sertaç, K. Experimental and Numerical Investigation of DARPA Suboff Submarine Propelled with INSEAN E1619 Propeller for Self-Propulsion. *J. Ship Res.* **2019**, *63*, 235–250.
17. Carrica, P.M.; Kerkvliet, M.; Quadvlieg, F.; Pontarelli, M.; Martin, J.E. CFD Simulations and Experiments of a Maneuvering Generic Submarine and Prognosis for Simulation of Near Surface Operation. In Proceedings of the 31st Symposium on Naval Hydrodynamics, Monterey, CA, USA, 11–16 September 2016.
18. Kim, H.; Ranmuthugala, D.; Leong, Z.Q.; Chin, C. Six-DOF simulations of an underwater vehicle undergoing straight line and steady turning manoeuvres. *Ocean Eng.* **2018**, *150*, 102–112. [CrossRef]
19. Coe, R.G. Improved Underwater Vehicle Control and Maneuvering Analysis with Computational Fluid Dynamics Simulations. Ph.D. Thesis, Virginia Polytechnic Institute and State University, Blacksburg, VA, USA, 2013.
20. Overpelt, B.B.N.; Anderson, B. Free running manoeuvring model tests on a modern generic SSK class submarine (BB2). In Proceedings of the Pacific International Maritime Conference, Sydney, Australia, 6–8 October 2015.
21. Zhou, G.; Ou, Y.; Gao, X.; Liu, R.J. Overset Simulations of Submarine's Emergency Surfacing Maneuvering in Calm Water and Regular Waves. *J. Ship Mech.* **2018**, *22*, 1471–1482.
22. Wu, L.; Feng, X.; Ye, Z.; Li, Y. Physics-Based Simulation of AUV Forced Diving by Self—Propulsion. *J. Shanghai Jiao Tong Univ.* **2021**, *55*, 290–296.
23. Carrica, P.M.; Kim, Y.; Martin, J.E. Vertical zigzag maneuver of a generic submarine. *Ocean Eng.* **2021**, *219*, 108386. [CrossRef]
24. Joubert, P.N. Some Aspects of Submarine Design, Part 1. Hydrodynamics, Defence Science and Technology Organisation, DSTO-TR-1622, October 2004. Available online: https://primoa.library.unsw.edu.au/primo-explore/fulldisplay?vid=UNSWC&tab=default_tab&docid=UNSW_ALMA21140087510001731&lang=en_US&context=L (accessed on 1 November 2021).
25. Joubert, P.N. Some Aspects of Submarine Design, Part 2. Shape of a Submarine 2026, Defence Science and Technology Organisation, DSTO-TR-1920, December 2006. Available online: https://citeseerx.ist.psu.edu/viewdoc/download?doi=10.1.1.508.5665&rep=rep1&type=pdf (accessed on 1 November 2021).
26. Watt, G.D. DRDC-Atlantic Research Centre. BB3: A Generic BB2 Based Submarine Design Using Sternplanes, Rudder, and Bowplanes. 2019. Available online: https://cradpdf.drdc-rddc.gc.ca/PDFS/unc341/p811112_A1b.pdf (accessed on 1 November 2021).
27. Pan, Y.; Zhang, H.; Zhou, Q. Numerical Prediction of Submarine Hydrodynamic Coefficients Using CFD Simulation. *J. Hydrodyn.* **2012**, *24*, 840–847. [CrossRef]
28. CD-Adapco. 2020 STAR CCM+ User's Guide Version 15.04. Available online: https://www.plm.automation.siemens.com/global/zh/products/simcenter/STAR-CCM.html (accessed on 1 November 2021).
29. Stern, F.; Wilson, R.; Shao, J. Quantitative V&V of CFD simulations and certification of CFD codes. *Int. J. Numer. Methods Fluids* **2006**, *50*, 1335–1355.
30. Zhang, N.; Shen, H.; Yao, H. Uncertainty analysis in CFD for resistance and flow field. *J. Ship Mech.* **2008**, *12*, 211.
31. Bradford, G.K.; Kevin, J.M. A semi-empirical multi-degree of freedom body force propeller model. *Ocean Eng.* **2019**, *178*, 270–282.
32. Oda, J.; Yamazaki, K. Technique to Obtain Optimum Strength Shape by the Finite Element Method: On Body Force Problem. *Trans. Jpn. Soc. Mech. Eng.* **1978**, *44*, 1141–1150. [CrossRef]
33. Kawamura, T.; Miyata, H.; Mashimo, K. Numerical simulation of the flow about self-propelling tanker models. *J. Mar. Sci. Technol.* **1997**, *2*, 245–256. [CrossRef]
34. Nakatake, K.; Sekiguchi, T.; Ando, J. Prediction of Hydrodynamic Forces Acting on Ship Hull in Oblique and Turning Motions by a Simple Surface Panel Method. In *Practical Design of Ships and Other Floating Structures*; Elsevier Science Ltd.: Amsterdam, The Netherlands, 2001; Volume 1, pp. 645–650.
35. Stern, F.; Yang, J.; Wang, Z.; Sadat-Hosseini, H.; Mousaviraad, M.; Bhushan, S.; Xing, T. Computational ship hydrodynamics: Nowadays and way forward. *Int. Shipbuild. Prog.* **2013**, *60*, 3–105.

36. Phillips, A.B.; Turnock, S.R.; Furlong, M. Comparisons of CFD simulations and in-service data for the self-propelled performance of an Autonomous Underwater Vehicle. In Proceedings of the 27th Symposium of Naval Hydrodynamics, Seoul, Korea, 5–10 October 2008.
37. Broglia, R.; Dubbioso, G.; Durante, D.; Di Mascio, A. Simulation of turning circle by CFD: Analysis of different propeller models and their effect on manoeuvring prediction. *Appl. Ocean Res.* **2013**, *39*, 1–10. [CrossRef]
38. Dubbioso, G.; Durante, D.; Di Mascio, A.; Broglia, R. Turning ability analysis of a fully appended twin screw vessel by CFD. Part II: Single vs. twin rudder configuration. *Ocean Eng.* **2016**, *117*, 259–271. [CrossRef]
39. Sezen, S.; Dogrul, A.; Delen, C.; Bal, S. Investigation of self-propulsion of DARPA Suboff by RANS method. *Ocean Eng.* **2018**, *150*, 258–271. [CrossRef]
40. Li, S.; Ye, J.; Zhang, H. Analysis of underwater fixed depth turning characteristic of X-rudder and C-rudder submarine. *J. Ship Mech.* **2020**, *24*, 1433–1442.
41. Han, K.; Cheng, X.; Huang, C.; Kangli, T. Impacts of Rudder Profiles on UV Maneuverability Based on Numerical Simulation. In Proceedings of the 30th International Ocean and Polar Engineering Conference, Virtual, 11 October 2020; OnePetro: Shanghai, China, 2020.
42. Uncertainty Analysis for Free Running Model Tests[S]. ITTC Recommended Procedures and Guidelines. 7.5-02-06-05:2014 Revision 00. Available online: https://www.ittc.info/media/8091/75-02-06-05.pdf (accessed on 1 November 2021).
43. Leong, Z.Q.; Piccolin, S.; Desjuzeur, M.; Ranmuthugala, D.; Renilson, M. Evaluation of the Out-of-Plane loads on a submarine undergoing a steady turn. In Proceedings of the 20th Australasian Fluid Mechanics Conference, Perth, Australia, 5–8 December 2016.